



OPEN

Future European Arctic limited under sustained global warming

Francesco De Rovere¹, Matteo Mastropiero¹, Johann H. Jungclaus², Myriam Khodri³, Angelo Rubino¹ & Davide Zanchettin¹✉

Atlantic domain towards the Arctic, driving rapid oceanic and ecological changes in the European Arctic. Using reanalyses and a multi-model ensemble of unperturbed and transient preindustrial, historical and future-scenario simulations, this study shows that modern initiated in the late nineteenth century, preceded by several preindustrial millennium. In the historical period, constructively to drive upper

Sea. Modern
vealing its exceptional

character in the context of the past millennium. However, , decoupling from pan-Arctic warming. The northward expansion of the Atlantic domain is hindered by the onset of a damping mechanism where the Atlantic-Arctic density gradient increases progressively, which sustains a countercurrent by baroclinic adjustment pushing the Arctic polar front southward. As the evolution of this density gradient is intertwined with the retreat of the sea-ice edge, a late-summer ice-free Barents Sea may mark the end of modern

The Arctic has been experiencing pervasive changes in recent decades across its marine, coastal and terrestrial environments¹, portrayed by the severe and rapid surface warming and sea-ice loss observed in the central Arctic^{2–4}. Arctic warming is progressing at a pace much faster than in the rest of the planet, a phenomenon which has become widely known as Arctic amplification of climate change⁵. Recently a ‘new’ phenomenon has emerged in the European Arctic –the area encompassing the Fram Strait and Barents Sea–, where seawater properties have evolved from a typical condition of a stratified water column with a layer of cold and fresh Arctic waters confining warm and salty Atlantic waters at intermediate depths⁶, to a more homogenous water column composed by warmer and saltier waters resembling Atlantic properties^{7,8}. This “Atlantification” of the European Arctic has been especially observed in the Barents Sea⁷, the West Spitsbergen Shelf and fjords^{9,10} and the area north of Svalbard¹¹ and has far-reaching influences on sea-ice formation and vertical mixing, hence on the local circulation, productivity and ecosystems^{12–14}.

Atlantification revolves around the following mechanisms. In the open-ocean and yearly ice-free areas, Atlantification has been explained by strengthened advective and diffusive heat transport convergence^{14,15} modulated by large-scale wind patterns¹⁶. In the marginal ice zones, it stems from weakened surface ocean heat losses due to atmospheric warming¹⁵, and reduced ocean stratification by weakened sea-ice advection¹³. Lateral transport of sea ice from the main Arctic basin toward the Barents Sea provides the lateral freshwater input necessary to keep the marginal ice zone in a cold and stratified state, dampening the upward heat and salt fluxes from the underlying Atlantic water layer¹⁷. In ice-covered areas, ocean heat advection and air-sea fluxes act together to drive a gradual warming of the upper ocean¹⁵. As a result of strengthened Atlantic water inflows, the area north of Svalbard and the Barents Sea is transitioning from an ice-covered to an ice-free region for longer periods during the year^{18–20}, which can initiate further reinforcement of the warming through the sea ice-albedo feedback. Mechanisms of Atlantification thus intertwine with or may represent a regional expression of Arctic amplification mechanisms involving cryosphere and ocean^{5,21–23}.

Characterization of the early development of Atlantification is limited by structured oceanographic observations and ocean reanalyses covering only the past few decades²⁴. Available paleoceanographic reconstructions and paleoclimate model simulations describing the initial phases of the Arctic response to global warming consistently depict the exceptional character and an early onset of modern surface ocean warming in

¹Department of Environmental Sciences, Informatics and Statistics, Ca’ Foscari University of Venice, Mestre, Italy. ²Max-Planck-Institut für Meteorologie, Hamburg, Germany. ³LOCEAN-IPSL, Sorbonne Université/CNRS/IRD/MNHN, Paris, France. ✉

the European Arctic via enhanced poleward heat-conductive conditions towards the Nordic Seas^{25,26} and the Arctic²¹. However, studies disagree on magnitude and timing of European Arctic warming^{27–29}, and only one study²⁹ explicitly invokes Atlantification to explain oceanographic changes reconstructed in the eastern Fram Strait. It remains therefore unclear whether reconstructed and simulated changes are truly descriptive of an expansion of the Atlantic domain in the European Arctic, rather than the regional expression of pan-Arctic changes largely independent from Atlantification.

An ongoing acceleration of Atlantification³⁰ and suggestions that it may continue in the future^{18,31} contribute to increasing scientific interest in this phenomenon. Atlantification, as pan-Arctic warming, is critically connected with changes in the stratification and vertical density distribution of the upper Arctic Ocean and changes in sea ice, which are known crucial factors controlling Arctic state and variability^{6,32–34}. Both also express the natural exposure of the Arctic environment to Atlantic forcing²¹. This phenomenological superposition calls for a careful framing of Atlantification toward an unambiguous fingerprinting of its historical and potential future impacts. This need is further stressed by the lack of quantitative estimates for the current magnitude of Atlantification.

Hence, this study provides a coherent historical and future perspective on the Atlantification by using ORAS5 ocean reanalyses covering the past six decades and a multi-model ensemble of climate simulations extending from the preindustrial millennium to the end of the twenty-first century (see Methods). A clustering algorithm applied on upper-ocean thermohaline properties is used to divide the European Arctic into two domains –Atlantic and Arctic– and build an Atlantification index, ATLi, that quantifies changes in the areal extent of the Atlantic domain in the European Arctic (see Methods). Accordingly, an increase in ATLi values describes Atlantification, whereas a decrease describes Arctification, that is, the Arctic domain gaining area at the expense of the Atlantic domain. ATLi accounts for the concomitant relative state of the Atlantic and Arctic oceans, thus accounting for their vast historical and projected changes, and allows surpassing limitations imposed by the severe model biases in ocean temperature and salinity known in the region^{35,36}. Our results show that modern Atlantification is rooted in late preindustrial times yet projected to stop after the 2050s due to an oceanic damping mechanism triggered by an increased density gradient between Atlantic and Arctic waters in the European Arctic.

Results

Modern

The clustering algorithm applied to ORAS5 yields the current Atlantic domain to mainly encompass the southern side of the European Arctic, the West Spitsbergen area, the area close to the Barents Sea Opening and the southern Barents Sea (Fig. 1a,c,e,g, red lines), where the Norwegian Atlantic and West Spitsbergen currents flow (supplementary Figure S1). The position of the Atlantic-Arctic boundary is robust against different considerations of the vertical structure of the water column (see Methods). The multi-model ensemble captures the gross spatial features of the modern (1981–2010) Atlantic-Arctic boundary, especially in its eastern branch (Fig. 1a,c,e,g, blue shading). There, the S-shaped profile in MPI-ESM1-2-LR and IPSL-CM6A-LR reflects a realistic representation of the flow of the Norwegian Atlantic and Spitsbergen Polar currents, whereas the more linear profile in MRI-ESM-2-0 and MIROC-ES2L suggests a too weak circulation in the area. Models diverge more regarding the typical position of the Atlantic-Arctic boundary in the Fram Strait, reflecting uncertainties in the simulation of the West Spitsbergen current.

Mean state biases in the Atlantic-Arctic boundary are reflected in a mean state bias in the areal extent of the Atlantic domain in the European Arctic that is ubiquitous across models (Fig. 2a). Models overestimate ATLi from reanalysis especially in the Fram Strait, whereas distributions overlap in the Barents Sea region –most relevant for Atlantification– within the 1.5 interquartile range, except for IPSL-CM6A-LR (supplementary Figure S2). Notwithstanding mean state biases, simulated ATLi anomalies encompass reanalyses during the observational period (Fig. 3b), illustrating model-data consistency in the temporal evolution of Atlantification. ATLi trends (period 1958–2014) consistently quantifies the progress of Atlantification in ORAS5 (0.7–1.4%/decade) and in the ensemble mean (0.9–1.2%/decade), supporting that the forced component is predominant since the second half of the twentieth century.

As expressed by pan-Arctic temperature, PAT (see Methods), the Arctic Ocean warms consistently across models and realizations during the historical period (Figs. 2, 3d). Ocean thermal inertia dampens high-frequency variability while highlighting multidecadal-to-centennial trends in PAT, which remain below 0.05 °C/decade in the ensemble mean during the historical period. Coherent decadal trends in ATLi and PAT indicate that Atlantification events historically occur during phases of pan-Arctic warming, while Arctification events occur during phases of pan-Arctic cooling (Fig. 3a,c). Multivariate regression of upper-ocean (0–200 m depth) temperature and salinity on ATLi and PAT supports that Atlantification and pan-Arctic warming constructively superposed in driving historical upper-ocean warming and salinification of the European Arctic, with comparable relative impacts (Fig. 4a,c, spatial fingerprints in supplementary Figures S3 and S4). The historical period thus features a tight coupling between local dynamics in the European Arctic and pan-Arctic properties.

Consistently across simulations and reanalyses, the Atlantic-Arctic boundary approximates the winter sea-ice edge but remains more locally confined than the latter through the year (Fig. 1b,d,f,h and supplementary Figures S5 and S6) maintained by buoyancy fluxes. The Atlantic-Arctic boundary position is therefore not a mere expression of sea-ice dynamics, although the latter contribute to explain the diversity of simulated behaviors.

Projected future evolution of

The ensemble coherence extends beyond the observational period, as the models yield a strongly consistent temporal evolution of the Atlantification across models and realizations over the whole *historical* and *ssp585/ssp245* experiments, independent of the future scenario considered. Following the initial stationary phase with lack of interdecadal trends from 1850 to the first quarter of the twentieth century, the ensemble-mean evolution of ATLi exhibits a progressive acceleration culminating around the mid-twenty-first century (Fig. 3b, *ssp245* in

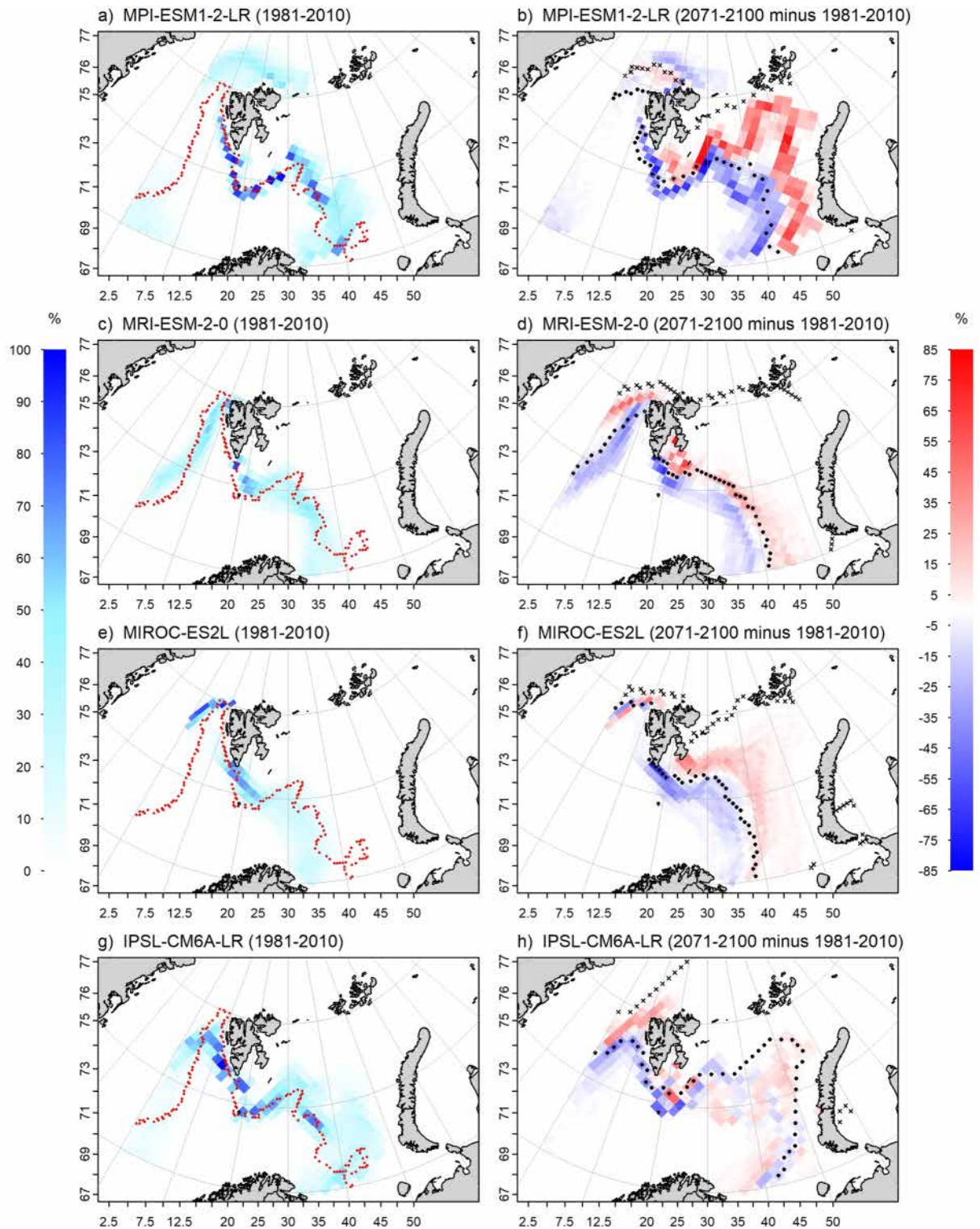


Fig. 1. Atlantic-Arctic boundary position in reanalysis and climate simulations. **(a,c,e,g)** Expected Atlantic-Arctic boundary position in the modern (1981–2010) period for ORAS5 ocean reanalyses (red dots) and climate simulations (shading) from MPI-ESM1-2-LR **(a)**, MRI-ESM-2-0 **(c)**, MIROC-ES2L **(e)** and IPSL-CM6A-LR **(g)**. **(b,d,f,h)** Change in the expected Atlantic-Arctic boundary position between modern and future (2071–2100, *ssp585* scenario) periods simulated by MPI-ESM1-2-LR **(b)**, MRI-ESM-2-0 **(d)**, MIROC-ES2L **(f)** and IPSL-CM6A-LR **(h)**. Red (blue) colors indicate areas where the front position is more (less) probable in the future compared to the modern period. Filled circles and crosses represent the position of the average sea-ice edge in March in the modern and future period, respectively.

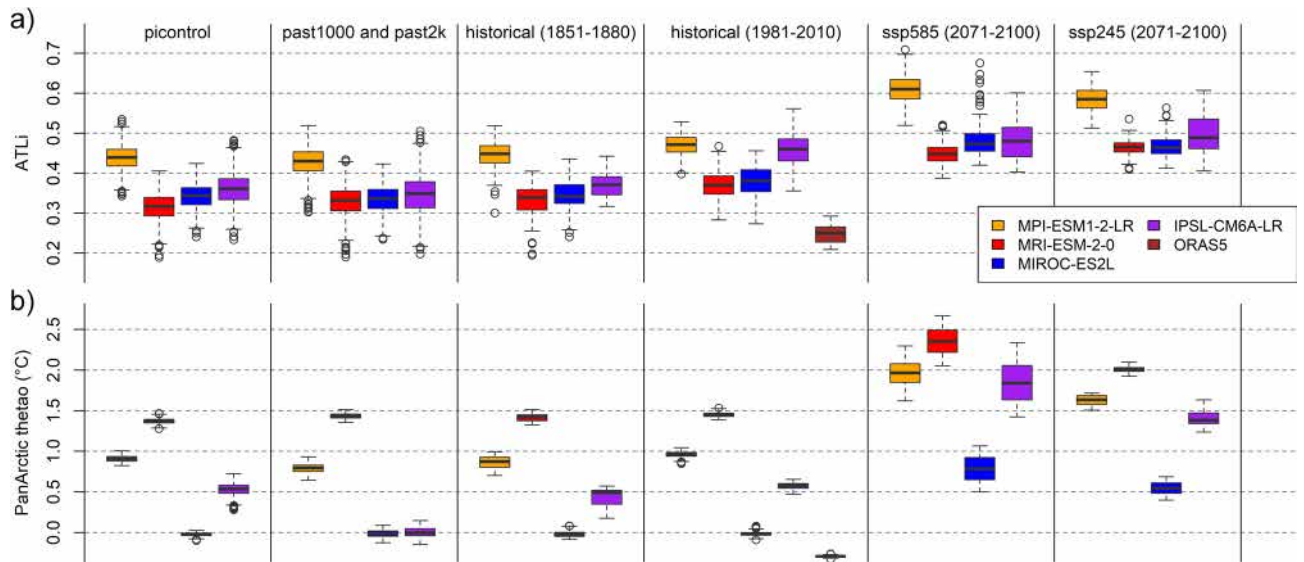


Fig. 2. Boxplots of single-model ensemble and reanalysis distributions of ATLi (a) and PAT (b) in various experiments. Shown are median (thick black line), interquartile range (IQR, boxes), $1.5 \times \text{IQR}$ (whiskers) and outliers (circles). Models are vertically aligned in panels a and b.

supplementary Figure S7). The Atlantic maximizes its areal gain around 2060, followed by a stationary phase until 2100 characterized by a northward displacement of the eastern branch of the Atlantic-Arctic boundary (Fig. 1b,d,f,h). This sustained Atlantification occurs across all models, realizations and scenarios (Fig. 2a), thus representing a forced response under global warming. Under *ssp585* conditions, MIROC-ES2L and MRI-ESM-2-0 yield similar peak ATLi values (0.45–0.50) but achieved through a small and homogeneous progression along the modern position in MIROC-ES2L, and a stronger progression along the northern branch of the Atlantic flow in MRI-ESM-2-0 (Fig. 1d,f). In IPSL-CM6A-LR the Atlantic domain exhibits a geographically incoherent progression yielding an areal gain of only about 5% (Fig. 1h). MPI-ESM1-2-LR yields the strongest future Atlantification (ATLi exceeding 0.50), associated with an advancement of the Atlantic similar to MRI-ESM-2-0 but extending further north (Fig. 1b). The simulated Atlantic-Arctic boundary evolution is even more diverse across models in the Fram Strait, further contributing to the ensemble spread of projected future Atlantification.

The strong projected (*ssp585*) sea-ice loss results in the European Arctic facing absence of sea ice in late summer in the second half of the twenty-first century and a substantial retreat of the sea-ice edge in winter at the end of the century, when in the Barents Sea it is confined to above around 80°N , that is, much north of the projected Atlantic-Arctic boundary position (Fig. 1b,d,f,h and supplementary Figure S8). This spatial detachment suggests that in a warmer world different mechanisms govern Arctic sea-ice dynamics and the Atlantic-Arctic boundary. The strong sea-ice melting can be interpreted within the framework of pan-Arctic warming. As expressed by PAT, Arctic warming accelerates around 2010 up to exceeding $0.1^\circ\text{C}/\text{decade}$ by 2030 and $0.2^\circ\text{C}/\text{decade}$ by the end of the twenty-first century. Despite the diversity of biases in the modern PAT climatology, the ensemble agrees on a future pan-Arctic warming of about 1°C under *ssp585* and 0.7°C under *ssp245* (Fig. 2b), suggesting that the destabilizing feedbacks that determine Arctic amplification are consistently still operative at the end of the twenty-first century under both scenarios. The rate of Atlantification increases since 2010 as pan-Arctic warming accelerates, until Atlantification detaches from pan-Arctic warming around 2060 (Fig. 3b,d). Pan-Arctic warming becomes predominant in driving an overall upper-ocean warming and freshening of the European Arctic (Fig. 4b,d), while Atlantification remains a significant contributor to temperature changes only in the eastern and north-eastern region (supplementary Figures S9 and S10). Therefore, Atlantification/Arcticification aligns with pan-Arctic warming/cooling in the historical period, but both phenomena decouple under sustained global warming.

Natural roots of

Preindustrial experiments under transient (*past1000/past2k*) and unperturbed (*piControl*) conditions allow framing modern and projected Atlantification, and its relation with pan-Arctic warming, in the context of natural climate variability. All models agree that Atlantification is already distinguishable from natural variability: ATLi values for the modern period are consistently significantly higher ($p_{\text{ranksum}} < 10^{-5}$) than transient late preindustrial (1851–1880) and unperturbed preindustrial values (Fig. 2a). However, modern Atlantification does not fully exceed the range of natural variability, as early-21st-century ATLi values remain occasionally below the 95th percentile of *piControl* values depicting intrinsic variability (supplementary Figure S11). This is expected to change under continued global warming, where future distributions for both *ssp585* and *ssp245* only overlap with intrinsic variability above its 95th percentile, except for IPSL-CM6A-LR. Accordingly, the exceptional character of modern Atlantification will be fully revealed in the next decades. Further pointing to the exceptional contribution of external forcing to modern Atlantification, non-smoothed ensemble-mean values

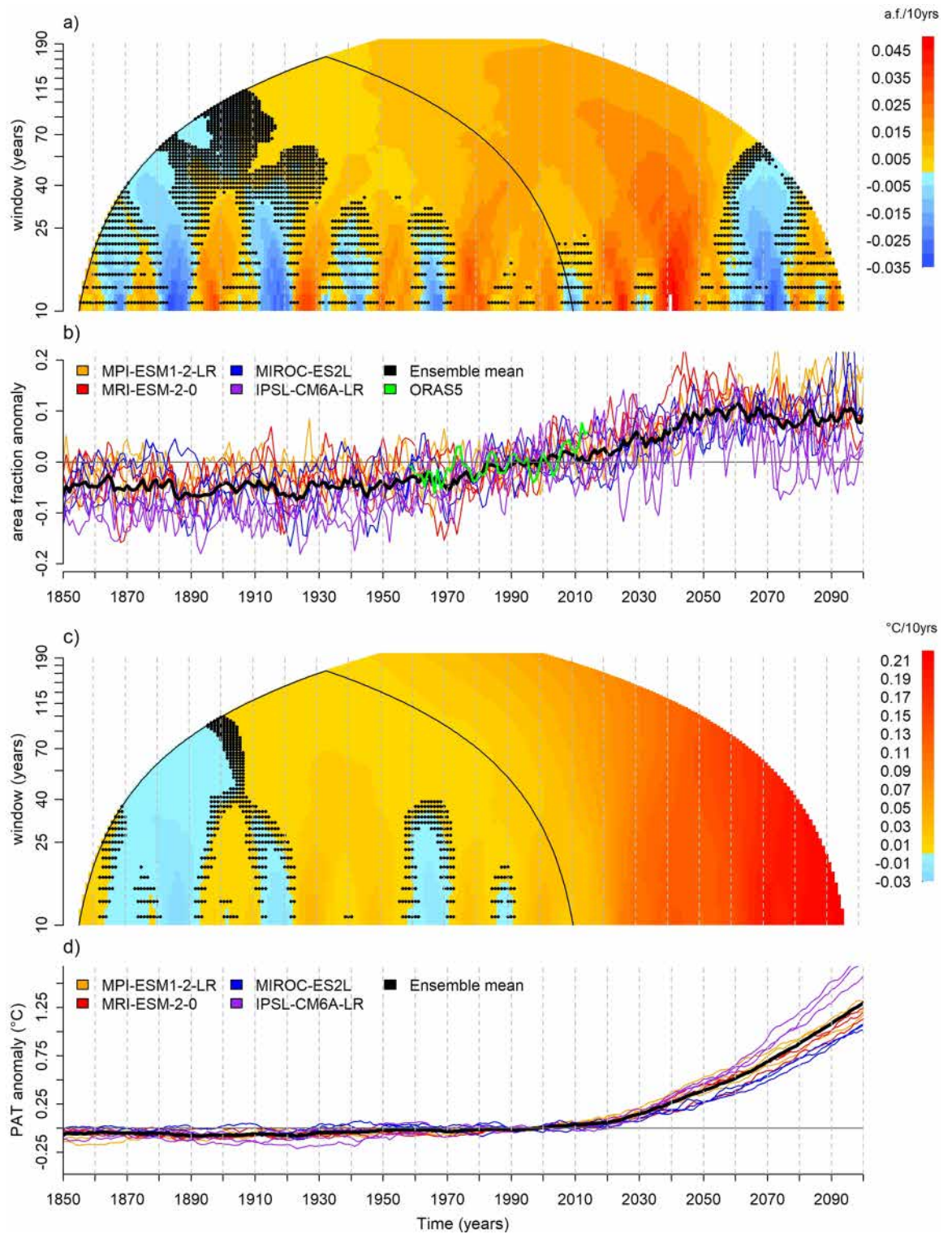


Fig. 3. Evolution and trends of Atlantification and Pan-Arctic warming in the historical and future scenario (*ssp585*) periods. Trend analysis of ATLi (a) and PAT (c) ensemble means. Trend coefficients with p-value > 0.05 are masked out with black dots. The black cone encompasses trends estimated for the historical period alone. Time series of ATLi (b) and PAT (d) for all considered models and realizations, as well as the multi-model ensemble mean (black line). The green line in panel (b) illustrates the ATLi time series from ORAS5. Data are anomalies referred to the 1981–2010 average.

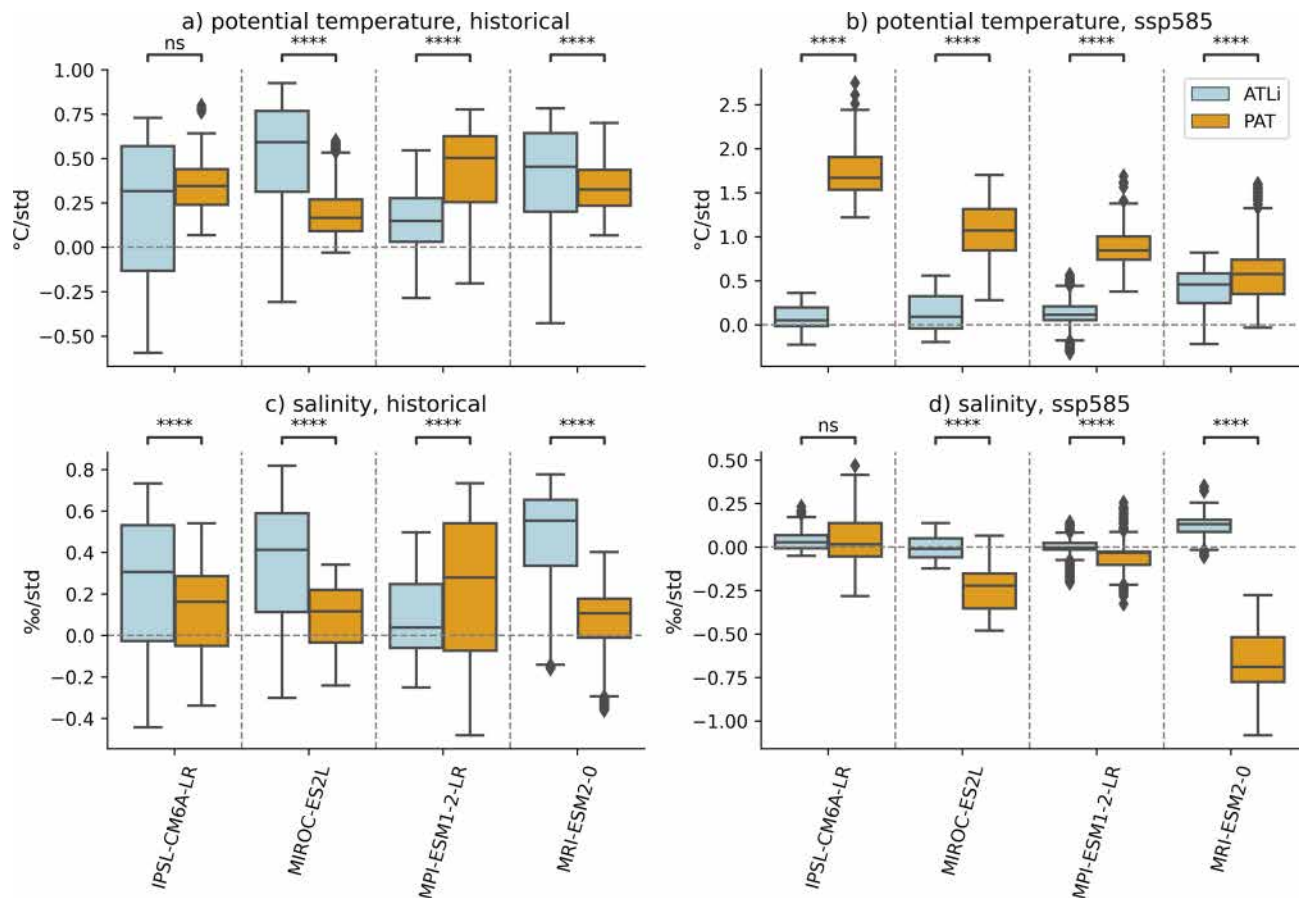


Fig. 4. Dependency of upper-ocean properties in the European Arctic on Atlantification and pan-Arctic warming. Box plots (line: median, box: interquartile range—IQR, whiskers: $1.5 \times \text{IQR}$, +: outliers) are for local (grid-point) regression coefficients in the European Arctic domain: (a,b) upper-ocean potential temperature and (c,d) upper-ocean salinity on ATLi and PAT calculated for the (a,c) *historical* and (b,d) *ssp585* experiments. Statistical significance, tested by means of a Mann–Whitney U-test, is reported in the stars above the plot as follows: $0.01 < p \leq 0.05$; $0.001 < p \leq 0.01$; $10^{-4} < p \leq 0.001$; $p \leq 10^{-4}$.

since 2007 exceed previous maxima during the whole preindustrial millennium and ensemble-mean trends in the historical period exceed preindustrial trends on all time scales (Fig. 5a,b).

In both individual simulations and the ensemble mean, preindustrial variability includes recurrent potent Atlantification and Arctification events, with duration and intensity comparable to modern Atlantification, revealing an almost symmetrical natural pattern of variability of the Atlantic–Arctic boundary around its natural climatological position (Fig. 5a,b and supplementary Figure S11). In all models, the ratio of ATLi standard deviations calculated for the *past1000/past2k* and *piControl* experiments only slightly exceeds the value of one (MPI-ESM1-2-LR: 1.12; MRI-ESM2-0: 1.04; MIROC-ES2L: 1.07; IPSL-CM6A-LR: 1.24). Arctification and Atlantification therefore pertain to the intrinsic features of climate variability, and this intrinsic component remains predominant for transient natural variability of the Atlantic–Arctic boundary. External forcing thus appears to primarily exert its role by setting the phase of variability generated by intrinsic dynamics.

A major Arctification episode is coherently simulated across models in the early nineteenth century (Fig. 5b), arguably as a forced response to the 1809–Tambora volcanic cluster³⁷. The beginning of modern Atlantification is rooted in the first half of the nineteenth century, if it also encompasses the recovery from an earlier Arctification episode. Spatial patterns further support a natural origin of modern Atlantification: the ensemble yields a coherent progression of the Atlantic–Arctic boundary across the Barents Sea from late preindustrial to modern times, whereas models largely disagree on changes in the Fram Strait (supplementary Figure S12), similar to what is obtained for projected future changes (Fig. 1b,d,f,h).

Consistent with indications from the *historical* experiment, the preindustrial period features a recurrent coexistence between Arctic warming/cooling episodes and Atlantification/Arctification throughout the *past1000/past2k* experiment (Fig. 5c,d). Global warming scenarios therefore project a disruption of a coherent natural behavior coupling Atlantification/Arctification and pan-Arctic warming/cooling that lasted on a millennial time scale.

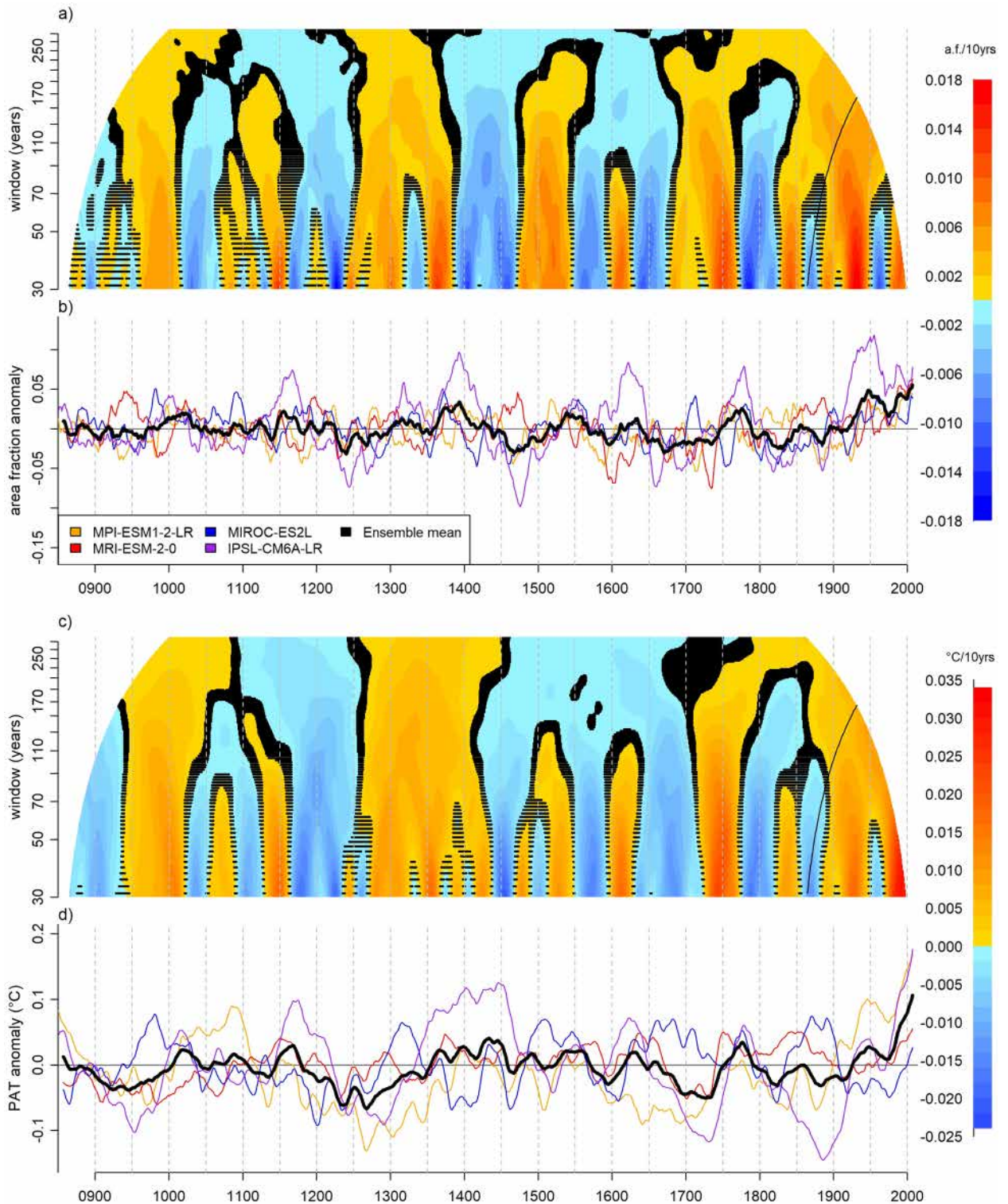


Fig. 5. Atlantification and Pan-Arctic warming in the climatic context of the last millennium. Trend analysis of ATLi (a) and PAT (c) ensemble means. Trend coefficients with p -value < 0.05 are masked out with a black dot. The black line cone encompasses trends estimated for the historical period alone. Time series of ATLi (b) and PAT (d) for all considered models, as well as ensemble mean (black line), for the historical and parent past1000/past2k experiments. All series are anomalies with respect to the period 850–2014, smoothed with a 15-year moving average. For IPSL-CM6A-LR, spurious trends of 0.002 1/century for ATLi and 0.04 °C/century for PAT are preliminarily removed from the data.

Dynamics of limited future

Consistently across ensemble members, upper-ocean warming accelerates in the European Arctic during the late twentieth century while salinity decreases starting from the early twenty-first century, both changes contributing to a decrease in upper-ocean density (Fig. 6a,b,c). This general tendency masks a differential upper-ocean warming in the Atlantic and Arctic domains: except for IPSL-CM6A-LR, the average seawater temperature gradient (Atlantic minus Arctic) increases substantially from the 1970s until peaking in the 2050s, indicating that the Atlantic domain warms at a faster rate compared to the Arctic domain (Fig. 6d). The co-occurrence of this peak with sea-ice free late summers in the European Arctic (supplementary Figure S8) points toward a potential central role of sea-ice dynamics. For instance, sea-ice albedo and ocean latent heat loss by the ocean due to sea-ice melting contribute to slower warming of the Arctic domain. From the 2050s onwards, when sea ice retreats north of the European Arctic (supplementary Figure S8), the Atlantic-Arctic temperature gradient weakens in all models, indicating that the Arctic domain warms faster than the Atlantic domain. The Atlantic-Arctic gradient in salinity slightly increases in the *historical* experiment, but trajectories diverge in *ssp585*, yielding near-zero ensemble-mean projected future trends (Fig. 6e). Consistently across ensemble members, the Atlantic-Arctic gradient in density remains stable until around 2020 and then becomes more negative –it strengthens– until around 2050, when it stabilizes again (Fig. 6f).

Therefore, the density decrease of Arctic waters is consistently slower than Atlantic waters in the ensemble, despite model specificities in the relative contributions of salinity and temperature changes. The spatial patterns of end-of-21st-century upper-ocean density anomalies further reveal ensemble consistent features and model specificities (Fig. 7a,b,c,d, shading). All models agree on seawater density decrease near eastern Svalbard, where the Spitsbergen Polar Current typically flows southward. Models disagree instead on the density decrease in the Central Bank and surrounding areas, which traces back on the diversity of simulated changes in the Atlantic-Arctic boundary. MPI-ESM1-2-LR and MIROC-ES2L yield the most consistent anomalous density gradients across the Atlantic-Arctic boundary in the Barents Sea, seen as alignment between the boundary position and the anomalous isopycnals. In IPSL-CM6A-LR Atlantic-Arctic gradients are weakest in the Central Bank, whereas they even have an opposite sign, i.e., negative Atlantic-Arctic anomalous gradient, in the southeastern basin.

These changes reflect altered ocean–atmosphere interactions in the region: the anomalous density pattern superposes in the Barents Sea on winter wind-stress-curl anomalies, especially in MPI-ESM1-2-LR and MRI-ESM2-0 (supplementary Figure S13); changes in the winter net surface freshwater fluxes also contribute to the density anomaly, consistently following across models a strengthening of their historical climatological pattern of precipitation minus evaporation (supplementary Figure S14). The retreat of the sea ice edge further contributes to enhanced surface ocean turbulent heat losses in the Arctic portion of the Barents Sea (supplementary Figure S15). The overall picture is that local atmosphere–ocean interactions and local wind forcing substantially contribute to the density gradient between Atlantic and Arctic waters in the European Arctic, where the effect is mediated by sea ice changes.

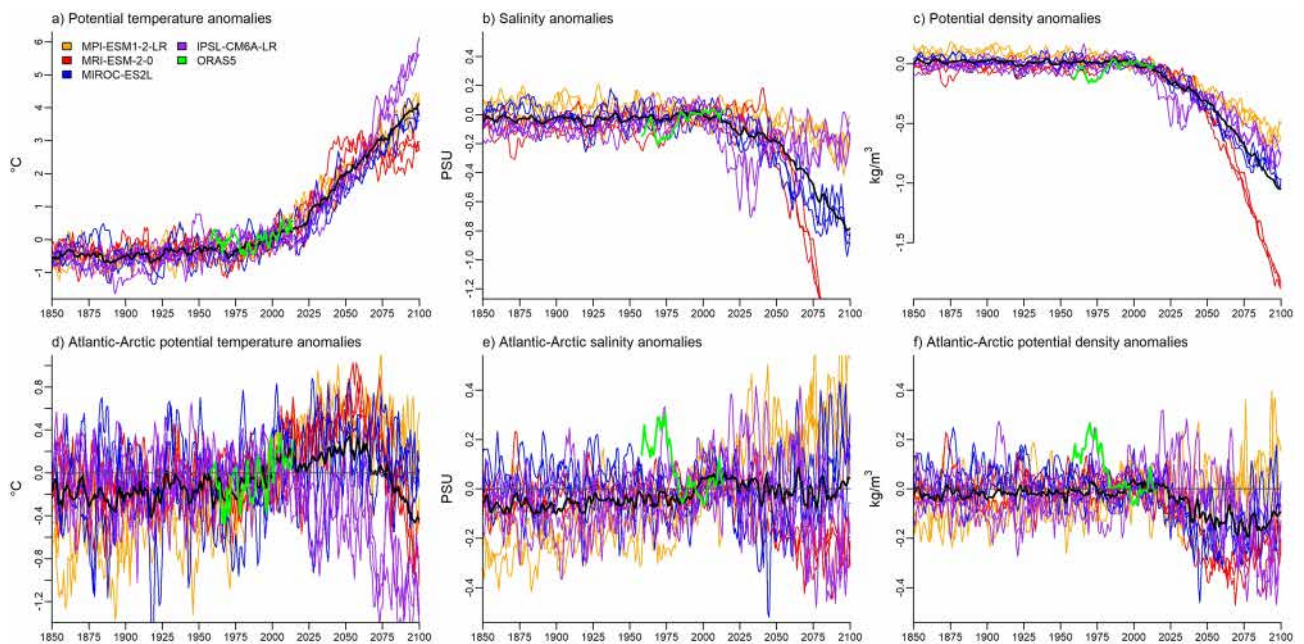


Fig. 6. Simulated evolution of oceanic conditions in the European Arctic in the historical and future scenario (*ssp585*) periods. Anomaly of the average potential temperature (a), salinity (b) and potential density (c) in the European Arctic. Anomaly of the differences in potential temperature (d) and potential density (f) between the Atlantic and the Arctic domain (Atlantic minus Arctic). Anomalies are calculated by subtracting the average value in the 1981–2010 period from the time series. Color code: MPI-ESM1-2-LR (orange), MRI-ESM2-0 (red), MIROC-ES2L (blue), IPSL-CM6A-LR (purple), ensemble mean (black).

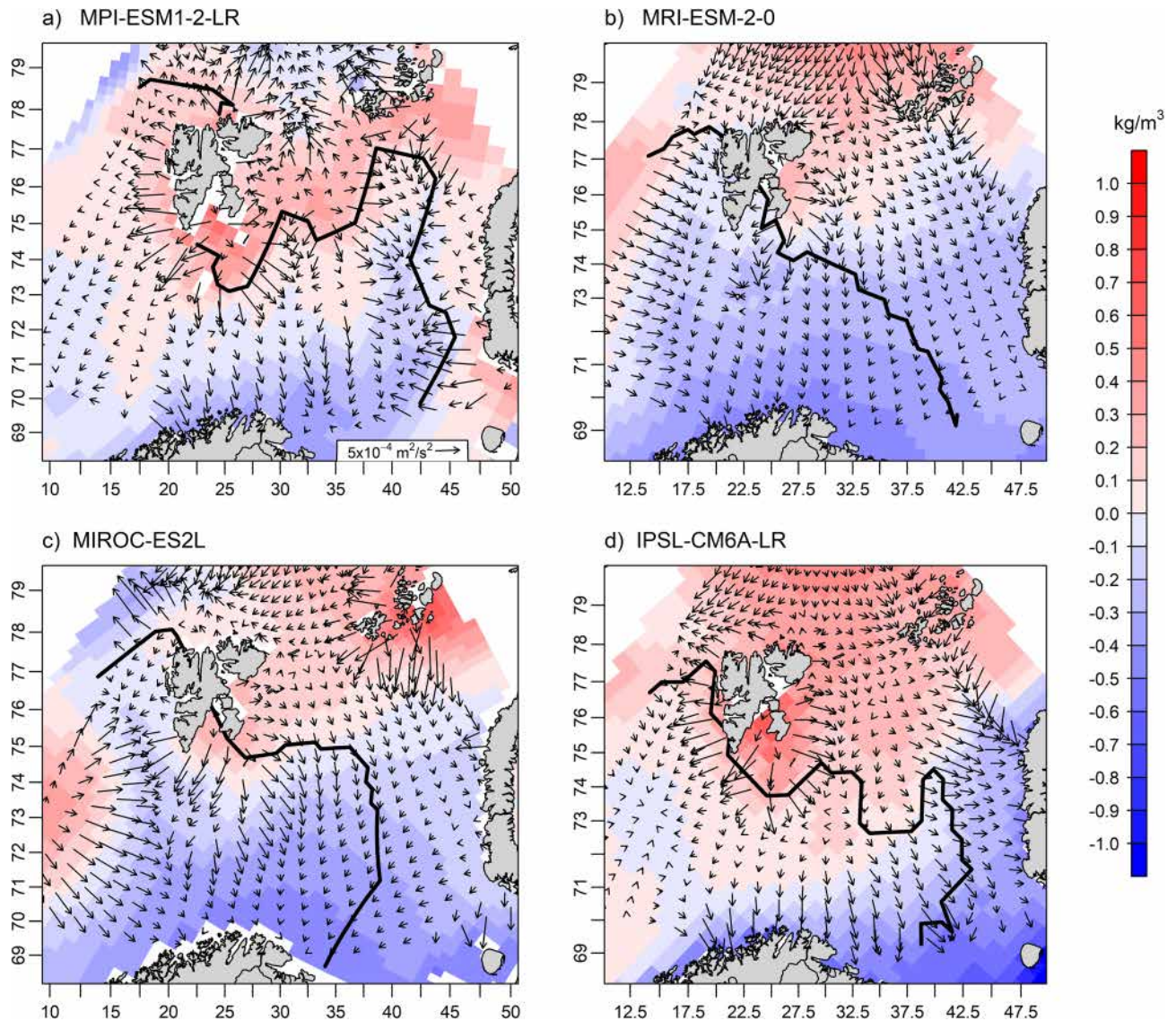


Fig. 7. Projected ocean circulation changes contrasting Atlantification. Upper-ocean density (color maps) and baroclinic pressure gradient (arrows) differences between the averages calculated over the future (2071–2100, *ssp585* experiment) and modern (1981–2010) periods for (a) MPI-ESM1-2-LR, (b) MRI-ESM-2-0, (c) MIROC-ES2L and (d) IPSL-CM6A-LR. For each model, the spatial average of the density difference is removed before mapping, amounting to (a) -0.52 kg/m^3 , (b) -1.32 kg/m^3 , (c) -0.78 kg/m^3 and (d) -0.71 kg/m^3 , hence an upper-ocean density decrease prevails over the European Arctic. Thick black lines correspond to the Atlantic-Arctic boundary position calculated for the future period.

The density anomalies are associated with a baroclinic pressure gradient force (Fig. 7 a,b,c,d, arrows). Besides model specificities –e.g., the southeastern basin in IPSL-CM6A-LR as mentioned above–, the ensemble consistently yields anomalous baroclinic pressure gradient force vectors in the area near the Atlantic-Arctic boundary that point south-westward, that is towards the Atlantic domain, which describes a countercurrent that contrasts Atlantification. Models lose coherence in strength and direction of the baroclinic pressure gradient force away from the Atlantic-Arctic boundary, which supports the interpretation that the dynamics described above pertain to a regional oceanic mechanism.

Large-scale oceanic precursors of the density anomalies are unclear. The ensemble yields a consistent 21st-century progressive weakening of the Atlantic meridional overturning circulation in its historical climatological core at tropical northern latitudes, but also stationary conditions or even temporary strengthening in its shallow polar component until around 2050 (supplementary Figure S16). In MPI-ESM1-2-LR these changes are reflected in latitudinal divergent trends in the meridional ocean heat transport driven by the overturning circulation, with reduction at tropical/mid latitudes and increase at subpolar/polar latitudes (supplementary Figure S17). These changes dominate the total meridional ocean heat transport and are associated with a shrinking and north-eastward intensification of the subpolar gyre with respect to its historical climatology (supplementary Figure S18a). The subpolar gyre also strengthens in MRI-ESM-2-0, but with different magnitude and spatial pattern

compared to MPI-ESM1-2-LR, whereas IPSL-CM6A-LR yields a slowdown of the subpolar gyre (supplementary Figure S18b,c).

Discussion

Our quantitative assessment of modern Atlantification aligns with recent indications regarding its recent acceleration³⁰ and possible late-preindustrial root²⁹. Further, it reveals that modern Atlantification has a predominant forced component but will be hampered by an oceanic mechanisms triggered by the repercussions of sustained global warming in the Barents Sea region, where the Atlantic-Arctic density gradient strengthens progressively up to trigger an Atlantic-ward current that opposes Atlantification. This contrasts with previous indications that Atlantification will continue in the future^{18,31}, which we explain as previous assessments not fully disentangling Atlantification from the local effects of pan-Arctic warming and neglecting the dynamical coevolution of Atlantic and Arctic seawater properties. Improved constraints on the future evolution of Atlantification can benefit from addressing the following sources of uncertainty.

First, simulated historical evolutions and projected changes are affected by climate model biases influencing the hydrography of the Arctic and Atlantic sub-polar regions^{35,36,38,39}. Model consistency therefore partly reflects shared biases, which remains an enduring issue. Besides recent use of similar ensembles^{37,40}, we stress the diversity of model behaviors in our ensemble: model coherency regarding the projected future dampening of Atlantification comes with model diversity regarding onset, magnitude and duration of the modern Atlantification, relative roles of seawater temperature and salinity for density changes, and different strengths of pan-Arctic warming seen in the diversity of projected future trajectories of Arctic seawater temperatures (Fig. 2c). Ultimately, this model diversity reflects critical differences in equilibrium climate sensitivities. IPSL-CM6A-LR, with the strongest climate sensitivity⁴¹, pan-Arctic warming and sea-ice loss in the Barents Sea (supplementary Figure S8), yields the strongest damping of Atlantification. This aligns with our general conclusion that Atlantification is damped under sustained global warming and that it is the relative states of Atlantic and Arctic oceans that matter for the underlying mechanism.

We stressed the potential role of air-sea interactions mediated by sea-ice melting for the increased Atlantic-Arctic density gradient and the consequent baroclinic adjustment in the Barents Sea, based on the consistent ensemble co-evolution between density gradient, surface freshwater and turbulent heat fluxes and sea-ice cover anomalies, and on basic physical arguments such as albedo and latent heat of melting effects. Differential lateral heat advection^{18,21}, partly triggered or at least sustained by changes in the large-scale North Atlantic ocean circulation, may be also part of the mechanism: the strengths of the gyre and overturning circulations can affect Atlantification by regulating the heat transport towards the Arctic²¹ while responding to Atlantification through, e.g., changes in local mechanisms of dense water formation⁴². The overturning and gyre responses diagnosed here for MPI-ESM1-2-LR are consistent with the model oceanic fingerprint of a warming climate⁴³ and contribute to enhanced poleward heat transport at high latitudes. However, whereas the multi-model ensemble agrees on the general overturning response, substantial discrepancies affect the subpolar gyre evolution. Also, the role of atmospheric heat transports remains unknown. This complexity and model diversity prevents pinpointing a remote origin of our proposed mechanism, further stressing the need to better understand the intertwining of the local ocean circulation, winds and sea-ice dynamics¹⁸ with the large-scale coupled gyre and overturning circulations⁴⁴ to improve constraints on the future evolution of Atlantification.

Remaining open questions concern the impacts of Atlantification beyond the European Arctic considered here¹². Fingerprinting impacts in northern basins, such as the Laptev Sea or the Amundsen Basin, may be critical to fully unravel the future of Atlantification. Then, understanding the natural functioning of Arctification and Atlantification expressed in transient and unperturbed preindustrial simulations bridges with the scientific challenge of robustly reconstructing Atlantification before the observational period using proxy data. We remark the broad symmetry between Arctification and Atlantification in the evolution of our Atlantification index in preindustrial times, but more details are needed to support the suggestion that both phenomena pertain to the same underlying mechanism.

In conclusion, this study sheds light on the strong historical relevance of the Atlantification in terms of both magnitude and duration of its effects in the European Arctic, and reveals how its future development may be short lived under continued warming of the planet. As demonstrated here for Atlantification, this reminds us that emerging or changing Earth system phenomena may be an impactful yet temporary manifestation of competing dynamics and feedbacks during certain phases of the transient climate response. This, in turn, requires a robust assessment not only of expected future but also remote past evolutions.

Methods

Data

Seawater temperature and salinity are retrieved from the Ocean Reanalysis System 5 (ORAS5) dataset⁴⁵, which provides global ocean and sea-ice reanalysis monthly-mean data prepared by the European Centre for Medium-Range Weather Forecasts OCEAN5 ocean analysis-reanalysis system⁴⁶. ORAS5 performs among the best ocean reanalyses regarding Arctic thermohaline properties, especially sea-surface salinity and its seasonality^{24,47,48}. ORAS5 data covering the period 1957–2014 are used to characterize modern Atlantification and define an observational Atlantification index (ATLi), defined below, that quantitatively describes the evolution of the phenomenon in recent decades. The data also serves as an observational reference for model evaluation. The ORAS5 grid (approximate horizontal resolution of 12 km in the study domain) is preliminarily interpolated on a regular grid with nominal 0.5° resolution to align with the typical model resolution.

This study leverages climate model data sourced from the Coupled Model Intercomparison Project Phase 6, CMIP6⁴⁹, and the Paleoclimate Model Intercomparison Project Phase 4, PMIP4⁵⁰, initiatives. Four-dimensional

fields of seawater potential temperature (CMIP6 output variable name: *thetao*) and seawater salinity (*so*) are retrieved and preprocessed by first interpolating the data at selected depths (from 10 to 190 m depth, every 10 m) and then vertically averaging to yield three-dimensional fields, which are finally averaged in time at a yearly frequency. The chosen thickness of the upper-ocean layer encompasses depths where Arctic and Atlantic waters are known to interact in the region^{13,14}. We tested other thicknesses in the range 10–300 m depth without obtaining significant changes in the results (not shown). Sea-ice area fraction (*sic*) data are used to examine the Arctic sea-ice edge.

The main analysis focuses on the 1850–2100 period covered by the *historical* and shared socio-economic pathways (*ssp*) scenario experiments, including *ssp585*, which yields a sustained warming signal throughout the twenty-first century, and the milder *ssp245* currently considered to provide for more realistic projected climates⁵¹. In addition, past Atlantification events are analyzed through available PMIP4 *past1000* and *past2k* simulations, including their continuation into the historical period described by their corresponding *historical* simulations.

Four models provide output for the *past1000/past2k* experiment and therefore contribute to our multi-model ensemble: the CMIP6 version of the Institut Pierre-Simon Laplace coupled atmosphere–ocean general circulation model (IPSL-CM6A-LR)⁵², the Model for Interdisciplinary Research on Climate, Earth System version2 for Long-term simulations (MIROC-ES2L)⁵³, the Max-Planck-Institute Earth System Model version 1.2 in its low-resolution version (MPI-ESM1-2-LR)⁵⁴, and the Meteorological Research Institute Earth System Model Version 2.0 (MRI-ESM-2-0)⁵⁵. Details regarding the models, experiments, and realizations employed in this study are outlined in supplementary Table S1. The models contributing to the *past1000/past2k* ensemble provide a coherent description of natural multidecadal oceanic³⁷ and atmospheric⁴⁰ variability in the North Atlantic sector. CMIP6 models are known to weakly represent the Atlantic water layer, which is typically found to be too deep and thick in simulations^{38,39}.

In CMIP6 models, seasonal biases in Arctic sea-ice climatology trace back to biases in various processes, including atmospheric and oceanic circulation³⁵ and sea-ice growth and melt fluxes³⁶. Models in our ensemble consistently show a warm bias over the southern Norwegian Sea, largest in MPI-ESM1-2-LR, but they disagree on magnitude and sign of biases in the eastern part of the European Arctic, where, for instance, MRI-ESM-2-0 shows vanishing errors and MIROC-ES2L a cold bias over extensive areas (supplementary Figure S19). There is also a tendency of the Atlantic domain to be slightly saltier in models than in reanalyses, but the largest salinity biases are in the northern margins of the Barents Sea (supplementary Figure S20). Temperature-salinity profiles further depict model biases in the climatological vertical structure of the upper-ocean column in Atlantic and Arctic waters in the European Arctic (supplementary Figure S21a,b). The ensemble profiles encompass reanalyses for the modern period, typically within ranges of ± 1 °C for temperature and ± 0.2 PSU for salinity for subsurface and deeper layers for both Arctic and Atlantic waters. Especially in layers approaching 300 m of depth, however, no model overlaps with reanalyses meaning that systematic errors in individual models tend to cancel out in the ensemble mean but no individual model represents the vertical structure of Arctic and Atlantic water columns. MIROC-ES2L stands out for its low salinity waters in the Atlantic and around 200 m of depth in the Arctic, where the other models are too salty; IPSL-CM6A-LR stands out for its overly warm and fresh surface waters in the Arctic. The vertical structure of thermohaline gradients between Atlantic and Arctic waters is better represented with ensemble largely overlapping with reanalyses (supplementary Figure S21c), meaning that individual models better represent Atlantic-Arctic gradients than Atlantic and Arctic properties. We exploit this feature to calculate an index for Atlantification.

Methods

Cluster analysis to determine the Atlantic-Arctic boundary position

First, CMIP6/PMIP4 and ORAS5 native grids are geographically subsetted in the European Arctic area that we define as comprising the eastern Fram Strait and the Barents Sea (70–85°N latitude and 0–60°E longitude). For each of the gridded temperature and salinity datasets, two anomaly fields are calculated, defined as local deviations from two reference points, one in the Atlantic domain and one in the Arctic domain. For each year, each anomaly field therefore measures the distances of the local seawater properties from the concomitant state of either the Atlantic or the Arctic ocean. The four anomalous fields are fed into a K-means cluster analysis with two groups: the Atlantic domain and the Arctic domain. We therefore expect two water masses to be always present in the region. Since seawater properties of both domains undergo large spatial and temporal variations, the algorithm does not impose any a priori conditions on the two clusters regarding ranges of temperature and salinity, and spatial extent (see supplementary Figure S21d–f for projected temperature-salinity profiles for Arctic and Atlantic waters, and associated gradients). The two reference points used for calculating anomalous fields consistently fall within the Atlantic and Arctic. This outcome is drawn from an initial cluster analysis of absolute potential temperature and salinity fields conducted over all considered years.

The Atlantic-Arctic boundary position is the area encompassing Atlantic grid cells with at least one Arctic grid cell among their four neighbour grid cells. The climatological position of the Atlantic-Arctic boundary in the late preindustrial, modern and future periods is determined for each model in terms of the local ensemble-mean frequency of occurrence of the boundary within the European Arctic. For each grid cell in the domain, this is calculated by summing up the total annual occurrences of the front in the grid cell, across all realizations, divided by the product of realizations and years in the considered period. Expected changes in the climatological front position between different periods are calculated as the difference between their associated ensemble-mean frequencies of occurrence.

In its main application, the clustering neglects an explicit consideration of the vertical structure of water masses, a known important aspect of Atlantification³⁵. However, in the region and depths relevant for Atlantification, the Atlantic domain is typically characterized by a nearly homogeneous column whereas the

Arctic domain exhibits a significant vertical gradient in both temperature and salinity. Hovmöller diagrams of vertical profiles confirm that, for the reanalyses and simulations employed here, vertically-averaged upper-ocean temperature and salinity fields retain the significantly different three-dimensional information for the two domains (supplementary Figures S22 and S23 for MPI-ESM1-2-LR, results are similar for the other models). An extended cluster analysis that explicitly accounts for the vertical structure of the water column (0–200 m of depth) and encompassing various hypotheses about stratification confirms the robustness of our approach for both, reanalyses and climate simulations (supplementary Figures S24 and S25).

Indices

The Atlantification index, ATLi, is defined to overcome limitations by model biases. It is based on the cluster analysis described above, where the Atlantic and Arctic domains in the European Arctic are identified based on the relative similarity of local upper-ocean temperature and salinity with concomitant properties of Atlantic and Arctic water masses. ATLi is defined as the area fraction occupied by the Atlantic domain in the European Arctic. ATLi is computed for each of the considered years, realizations and experiments. The robustness of the index is supported by the climatological position of the Atlantic-Arctic boundary in ORAS5 (Fig. 1) largely agreeing with qualitative descriptions of the Arctic oceanic front position from existing literature^{13,15,18,56}, notwithstanding margins of improvements in current reanalyses regarding Arctic circulation and associated water mass distributions²⁴.

Pan-Arctic temperature (PAT) is used to quantify warming of the Arctic Ocean. PAT is calculated by volumetrically averaging potential temperature across all depths for oceanic grid points north of 70°N, where the latitudinal extent of the Arctic Ocean is chosen to include its smaller fringe seas ranges and the European Arctic.

The sea-ice edge is calculated as follows. For each experiment, the sea-ice areal fraction data are averaged across all considered realizations, and the presence of sea ice is then defined for those grid points where the sea-ice areal fraction exceeds 15%. For each year in the experiment, the sea-ice edge encompasses those grid cells featuring sea ice and having at least one ice-free grid cell among their four closest neighbouring cells.

Meridional ocean heat transports are calculated for MPI-ESM1-2-LR following^{21,43} as $\sum_z \sum_x v T c_p \rho dx dz$, where v is the meridional velocity component, T is temperature, c_p is specific heat capacity at constant pressure, ρ is density, and dz and dx represent, respectively, the integrals along depths and longitudes. The overturning (gyre) transport is associated with the zonal-mean (residual) component of the total meridional ocean heat transports.

Statistical analyses

A trend analysis is performed by calculating linear trends at all time steps using different time windows of width ranging from decadal (11 years) to bicentennial (199 years). The reference year for the local trend is the central year in the window and local trends affected by border effects are excluded.

Finally, we use a multivariate linear regression (Ordinary Least-Squares, OLS) model to disentangle the relative contributions of Atlantification and pan-Arctic warming to changes in upper-ocean temperature and salinity in the European Arctic. The multivariate linear regression is performed separately on temperature and salinity data for each realization in the *historical* and *ssp585* experiments (full period) and for each grid point, using the standardized ATLi and PAT as predictors. The regression coefficients for ATLi and PAT are then averaged across realizations for each model and experiment.

Data availability

ORAS5 ocean reanalyses are available from the Copernicus Climate Data Store (<https://cds.climate.copernicus.eu/datasets/reanalysis-oras5?tab=overview>). The gridded monthly output of CMIP6 and PMIP4 climate model simulations that provides the raw data for this study is available via the following ESGF portals: USA, PCMDI/LLNL (California)—<https://esgf-node.llnl.gov/search/cmip6/>; France, IPSL—<https://esgf-node.ipsl.upmc.fr/search/cmip6-ipsl/>; Germany, DKRZ—<https://esgf-data.dkrz.de/search/cmip6-dkrz/>; UK, CEDA—<https://esgf-in.dex1.ceda.ac.uk/search/cmip6-ceda/>. A derived dataset containing the ATLi time series and the runscript for ATLi calculation is provided at <https://doi.org/10.5281/zenodo.16739358>. Requests about the data used in this study can be addressed to Francesco De Rovere (francesco.derovere@unive.it).

Received: 23 June 2025; Accepted: 13 August 2025

Published online: 21 August 2025

References

1. Cassotta, S. et al. Special report on ocean and cryosphere in a changing chapter intergovernmental panel on climate change (IPCC). In *Chapter 3 Polar Issues* (eds Cassotta, S. et al.) (Cambridge University Press, 2022).
2. Chylek, P. et al. Annual mean Arctic amplification 1970–2020: Observed and simulated by CMIP6 climate models. *Geophys. Res. Lett.* **49** (13), e2022GL099371 (2022).
3. Onarheim, I. H. & Årthun, M. Toward an ice-free Barents Sea. *Geophys. Res. Lett.* **44** (16), 8387–8395 (2017).
4. Polyakov, I. V., Ballinger, T. J., Lader, R. & Zhang, X. Modulated trends in Arctic surface air temperature extremes as a fingerprint of climate change. *J. Clim.* **37** (8), 2381–2404 (2024).
5. Serreze, M. C. & Barry, R. G. Processes and impacts of Arctic amplification: A research synthesis. *Glob. Plan. Ch.* **77** (1–2), 85–96 (2011).
6. Aagaard, K., Coachman, L. & Carmack, E. On the halocline of the Arctic Ocean. *Deep Sea Res. A.* **28** (6), 529–545 (1981).
7. Barton, B. I., Lenn, Y.-D. & Lique, C. Observed Atlantification of the Barents Sea causes the Polar Front to limit the expansion of winter sea ice. *J. Phys. Oceanogr.* **48** (8), 1849–1866 (2018).
8. Skagseth, Ø. et al. Reduced efficiency of the Barents Sea cooling machine. *Nat. Clim. Ch.* **10** (7), 661–666 (2020).
9. De Rovere, F. et al. Water masses variability in inner Kongsfjorden (Svalbard) during 2010–2020. *Front. Mar. Sc.* **9**, 741075 (2022).

10. Strzelewicz, A., Przyborska, A. & Walczowski, W. Increased presence of Atlantic water on the shelf south-west of Spitsbergen with implications for the Arctic fjord Hornsund. *Prog. Oceanogr.* **200**, 102714 (2022).
11. Ivanov, V. et al. Arctic ocean heat impact on regional ice decay: A suggested positive feedback. *J. Phys. Oceanogr.* **46** (5), 1437–1456 (2016).
12. Ingvaldsen, R. B. et al. Physical manifestations and ecological implications of Arctic Atlantification. *Nat. Rev. Earth Environm.* **2** (12), 874–889 (2021).
13. Lind, S., Ingvaldsen, R. B. & Furevik, T. Arctic warming hotspot in the northern Barents Sea linked to declining sea-ice import. *Nat. Clim. Ch.* **8** (7), 634–639 (2018).
14. Polyakov, I. V. et al. Greater role for Atlantic inflows on sea-ice loss in the Eurasian Basin of the Arctic Ocean. *Science* **356** (6335), 285–291 (2017).
15. Asbjørnsen, H., Årthun, M., Skagseth, Ø. & Eldevik, T. Mechanisms underlying recent Arctic Atlantification. *Geophys. Res. Lett.* **47** (15), e2020GL088036 (2020).
16. Polyakov, I. V. et al. Fluctuating Atlantic inflows modulate Arctic atlantification. *Science* **381** (6661), 972–979 (2023).
17. Lind, S., Ingvaldsen, R. B. & Furevik, T. Arctic layer salinity controls heat loss from deep Atlantic layer in seasonally ice-covered areas of the Barents Sea. *Geophys. Res. Lett.* **43** (10), 5233–5242 (2016).
18. Årthun, M., Eldevik, T. & Smedsrud, L. H. The role of Atlantic heat transport in future Arctic winter sea ice loss. *J. Clim.* **32** (11), 3327–3341 (2019).
19. Onarheim, I. H., Smedsrud, L. H., Ingvaldsen, R. B. & Nilsen, F. Loss of sea ice during winter north of Svalbard. *Tellus A Dyn. Meteorol. Oceanogr.* **66** (1), 23933 (2014).
20. Smedsrud, L. H., Ingvaldsen, R., Nilsen, J. E. Ø. & Skagseth, Ø. Heat in the Barents Sea: transport, storage, and surface fluxes. *Oce. Sc.* **6** (1), 219–234 (2010).
21. Jungclaus, J. H., Lohmann, K. & Zanchettin, D. Enhanced 20th-century heat transfer to the Arctic simulated in the context of climate variations over the last millennium. *Clim. Past* **10** (6), 2201–2213 (2014).
22. Dai, A., Luo, D., Song, M. & Liu, J. Arctic amplification is caused by sea-ice loss under increasing CO₂. *Nat. Comm.* **10** (1), 121 (2019).
23. Previdi, M., Smith, K. L. & Polvani, L. M. Arctic amplification of climate change: A review of underlying mechanisms. *Environm. Res. Lett.* **16** (9), 093003 (2021).
24. Hoffman, E. L., Subrahmanyam, B., Trott, C. B. & Hall, S. B. Comparison of freshwater content and variability in the arctic ocean using observations and model simulations. *Rem. Sens.* **15** (15), 3715 (2023).
25. Hátún, H., Sandø, A. B., Drange, H., Hansen, B. & Valdimarsson, H. Influence of the Atlantic subpolar gyre on the thermohaline circulation. *Science* **309** (5742), 1841–1844 (2005).
26. Koul, V., Schrum, C., Düsterhus, A. & Baehr, J. Atlantic inflow to the North Sea modulated by the subpolar gyre in a historical simulation with MPI-ESM. *J. Geophys. Res. Oce.* **124** (3), 1807–1826 (2019).
27. Spielhagen, R. F. et al. Enhanced modern heat transfer to the arctic by warm atlantic water. *Science* **331** (6016), 450–453 (2011).
28. Spooner, P. T. et al. Exceptional 20th century ocean circulation in the Northeast Atlantic. *Geophys. Res. Lett.* **47** (10), e2020GL087577 (2020).
29. Tesi, T. et al. Rapid Atlantification along the Fram Strait at the beginning of the 20th century. *Sc. Adv.* **7** (48), eabj2946 (2021).
30. Polyakov, I. V. et al. Atlantification advances into the Amerasian Basin of the Arctic Ocean. *Sc. Adv.* **11** (8), eadq580 (2025).
31. Dörr, J., Årthun, M., Eldevik, T. & Madonna, E. Mechanisms of regional winter sea-ice variability in a warming Arctic. *J. Clim.* **34** (21), 8635–8653 (2021).
32. Farmer, J. R. et al. Arctic Ocean stratification set by sea level and freshwater inputs since the last ice age. *Nat. Geosc.* **14** (9), 684–689 (2021).
33. Muilwijk, M. et al. Divergence in climate model projections of future Arctic Atlantification. *J. Clim.* **36** (6), 1727–1748 (2023).
34. Wang, Q. et al. Recent emergence of Arctic atlantification dominated by climate warming. *Sci. Adv.* **10**, eadq5235 (2024).
35. Frankignoul, C., Raillard, L., Ferster, B. & Kwon, Y.-O. Arctic september sea ice concentration biases in CMIP6 models and their relationships with other model variables. *J. Clim.* **37** (16), 4257–4274 (2024).
36. West, A. E. & Blockley, E. W. CMIP6 models overestimate sea ice melt, growth and conduction relative to ice mass balance buoy estimates. *Geosci. Model Dev.* **18**, 3041–3064. <https://doi.org/10.5194/gmd-18-3041-2025> (2025).
37. Fang, S. et al. The role of small to moderate volcanic eruptions in the early 19th century climate. *Geophys. Res. Lett.* **50** (22), e2023GL105307 (2023).
38. Khosravi, N. et al. The Arctic ocean in CMIP6 models: Biases and projected changes in temperature and salinity. *Earth Fut.* **10** (2), e2021EF002282 (2022).
39. Shu, Q. et al. Arctic Ocean Amplification in a warming climate in CMIP6 models. *Sc. Adv.* **8** (30), eabn9755 (2022).
40. Villamayor, J. et al. Sahel droughts induced by large volcanic eruptions over the last millennium in PMIP4/past1000 simulations. *Geophys. Res. Lett.* **50**, e2022GL101478 (2023).
41. Zanchettin, D. et al. Effects of forcing differences and initial conditions on inter-model agreement in the VolMIP volc-pinatubofull experiment. *Geosci. Model Dev.* **15**, 2265–2292 (2022).
42. Årthun, M. et al. Atlantification drives recent strengthening of the Arctic overturning circulation. *Sci. Adv.* **11**, eadu1794. <https://doi.org/10.1126/sciadv.adu1794> (2025).
43. Ghosh, R. et al. Two distinct phases of North Atlantic Eastern Subpolar Gyre and warming hole evolution under global warming. *J. Clim.* **36**, 1881–1894 (2023).
44. Mimi, M. S. & Liu, W. Atlantic meridional overturning circulation slowdown modulates wind-driven circulations in a warmer climate. *Comm. Earth Environm.* **5**, 727 (2024).
45. Copernicus Climate Change Service. ORAS5 global ocean reanalysis monthly data from 1958 to present. *ECMWF* <https://doi.org/10.24381/CDS.67E8EEB7> (2021).
46. Zuo, H., Balmaseda, M. A., Tietsche, S., Mogensen, K. & Mayer, M. The ECMWF operational ensemble reanalysis–analysis system for ocean and sea ice: A description of the system and assessment. *Oce. Sc.* **15** (3), 779–808 (2019).
47. Carton, J. A., Penny, S. G. & Kalnay, E. Temperature and salinity variability in the SODA3, ECCO4r3, and ORAS5 Ocean Reanalyses, 1993–2015. *J. Clim.* **32** (8), 2277–2293 (2019).
48. Hall, S. B., Subrahmanyam, B. & Morison, J. H. Intercomparison of Salinity Products in the Beaufort Gyre and Arctic Ocean. *Remote Sens.* **14** (1), 71 (2021).
49. Eyring, V. et al. Overview of the coupled model intercomparison project phase 6 (CMIP6) experimental design and organization. *Geosc. Mod. Develop.* **9** (5), 1937–1958 (2016).
50. Jungclaus, J. H. et al. The PMIP4 contribution to CMIP6 – Part 3: The last millennium, scientific objective and experimental design for the PMIP4 simulations. *Geosci. Model Dev.* **10**, 4005–4033 (2016).
51. Pielke, R. Jr. et al. Plausible 2005–2050 emission scenarios project between 2 degC and 3 degC of warming by 2100. *Environ. Res. Lett.* **17**, 024027 (2022).
52. Boucher, O. et al. Presentation and evaluation of the IPSL-CM6A-LR climate model. *J. Adv. Mod. Earth Sys.* **12** (7), e2019MS002010 (2020).
53. Hajima, T. et al. Development of the MIROC-ES2L Earth system model and the evaluation of biogeochemical processes and feedbacks. *Geosci. Model Dev.* **13**, 2197–2244 (2020).

54. Mauritsen, T. et al. Developments in the MPI-M earth system model version 1.2 (MPI-ESM1.2) and its response to increasing CO₂. *J. Adv. Mod. Earth Sys.* **11** (4), 998–1038 (2019).
55. Yukimoto, S. et al. The Meteorological research institute earth system model version 2.0, MRI-ESM2.0: Description and basic evaluation of the physical component. *J. Meteorol. Soc. Jap. Ser. II* **97** (5), 931–965 (2019).
56. Muilwijk, M., Smedsrud, L. H., Ilicak, M. & Drange, H. Atlantic water heat transport variability in the 20th century arctic ocean from a global ocean model and observations. *J. Geophys. Res. Oce.* **123** (11), 8159–8179 (2018).

Acknowledgements

This research was funded by the project Next-GenerationEU—PNRR – M.4 C.2, INVESTIMENTO 1.1—PRIN22 2022CCRN7R, “ATTRACTION—ATlantificaTion dRiven by polAr-subpolar ConnecTIONS”, CUP: H53D23001550006. Figure S1 was produced using the PlotSvalbard R package. The OLS regression has been performed using the Scikitlearn python library. We thank Helmuth Haak for help in the calculation of ocean heat transports.

Author contributions

Conceptualization: D.Z.; Data curation: F.D.R.; Formal analysis: D.Z., F.D.R., M.M.; Funding acquisition: D.Z.; Investigation: D.Z., F.D.R., M.M., A.R.; Methodology: D.Z., F.D.R., A.R.; Writing—original draft: D.Z., F.D.R., M.P.; Discussion: D.Z., F.D.R., M.M., A.R., J.H.J., M.K.; Revision: D.Z., F.D.R., J.H.J.

Declarations

Competing interests

The authors declare no competing interests.

Additional information

Supplementary Information The online version contains supplementary material available at <https://doi.org/10.1038/s41598-025-16161-8>.

Correspondence and requests for materials should be addressed to D.Z.

Reprints and permissions information is available at www.nature.com/reprints.

Publisher’s note Springer Nature remains neutral with regard to jurisdictional claims in published maps and institutional affiliations.

Open Access This article is licensed under a Creative Commons Attribution-NonCommercial-NoDerivatives 4.0 International License, which permits any non-commercial use, sharing, distribution and reproduction in any medium or format, as long as you give appropriate credit to the original author(s) and the source, provide a link to the Creative Commons licence, and indicate if you modified the licensed material. You do not have permission under this licence to share adapted material derived from this article or parts of it. The images or other third party material in this article are included in the article’s Creative Commons licence, unless indicated otherwise in a credit line to the material. If material is not included in the article’s Creative Commons licence and your intended use is not permitted by statutory regulation or exceeds the permitted use, you will need to obtain permission directly from the copyright holder. To view a copy of this licence, visit <http://creativecommons.org/licenses/by-nc-nd/4.0/>.

© The Author(s) 2025